# Nanoscale

## PAPER

Check for updates

# Ultra-broadband depolarization based on directly-coupled quantum wire-to-well modulation and their aliasing effect for polarization-insensitive light-emitting diodes

Yuhong Wang,[a] Hanxu Tai,[a] Ruonan Duan,[a] Ming Zheng,[a] Yue Shi,[a] Jianwei Zhang,[b] Xing Zhang,[b] Yongqiang Ning[b] and Jian Wu ID *[a]

Nowadays, strained quantum structures have been widely used in various light-emitting devices with a variety of compounds for progressive applications. However, the lattice-mismatch-induced strains in the materials would cause a problem of polarization dependence for polarization-independent optical applications. To address this issue, in this paper we propose a novel ultra-broadband depolarization mechanism and approach based on a directly-coupled well–wire-hybrid nanostructure. It contains quantum wire-to-well modulation and their aliasing effects on strain, energy-band structure and optical gain to obtain independent and comparable bipolarization of optical signals. The material structure involves a special well and on-well quantum wires with gradually-changing band-gaps, which are formed by utilizing the indium (In)-segregation effect and the growth-orientation-dependent multi-atomic step effect. With this special hybrid nanostructure, the depolarization efficiency can be 95% higher than that of a single compressive-strained quantum well. A low polarization degree of 0.05 and a very small gain difference of $|G_{TE} - G_{TM}| < 1.3$ cm$^{-1}$ in different polarizations are achieved over a very broad gain bandwidth (870–950 nm) for an InGaAs material system. Therefore, this is a new chance for the development of ultra-broadband and polarization-insensitive optical applications.

## Introduction

Nowadays, it is well known that strained light-emitting devices use various III–V and II–VI compounds as active materials to cover a more extensive wavelength range,[1–3] such as InGaN (0.4–1.8 μm), AlGaAs (0.5–0.9 μm), InGaAs (0.9–3.4 μm), and InGaAsP (0.9–1.7 μm). Therefore, strained light-emitting devices have achieved a very wide range of applications in the areas of lighting,[4] disinfection systems,[5] medical applications,[6] panel displays,[7] optical communications,[8] and so on. Moreover, the strained devices can produce a unique polarization mode of optical signals for the polarization light requirement due to the degeneracy release of heavy-hole (HH) bands and light-hole (LH) bands in a quantum system.[9–11] This therefore increases the applicability of strained light-emitting devices. However, this type of device also conflicts with polariz-ation-independent (insensitive) optical applications, such as semiconductor optical amplifiers, fiber optic gyroscopes, and electro-absorption modulators.[12–14] Therefore, seeking out an effective depolarization solution and corresponding material structures is also very significant, to remove the polarization dependence of the strained device for polarization-insensitive applications.

In order to achieve this goal, strain modulation based on energy-band engineering is a popularly-used depolarization mechanism and approach to equalize HH and LH contributions in the valence band of the material, as the transverse electric (TE) polarization mode of the device mainly arises from carrier recombination between the conduction band and the HH band, while the transverse magnetic (TM) polarization mode comes from carrier recombination between the conduction band and the LH band.[11,15] For conventional compressive-strained and lattice-matched quantum-confined devices, as the TE optical signal is larger than the TM signal due to the strain and quantum size effects,[16] increasing the TM contribution is necessary to achieve polarization independence. This means that tensile-strained materials must be combined in the active structure to increase carrier recombination between the conduction band and the LH band.

*[a]School of Physics, Beihang University, Beijing 102206, China.
E-mail: jwu2@buaa.edu.cn
[b]State Key Laboratory of Luminescence and Application, Changchun Institute of Optics, Fine Mechanics and Physics, Chinese Academy of Sciences, Changchun 130033, China*

According to such a mechanism, some depolarization methods have been investigated in the past. These methods involve the use of tensile-strained barriers,[17] tensile-strained quantum wells,[11,18] delta-strained auxiliary layers,[19,20] hybrid-strain quantum wells,[21–24] and vertically-stacked quantum dots.[25–27] We notice that these previous approaches have a common point: that is, the whole active structure is some sort of combination of multiple quantum-confined layers that have different types of strain or a mixture of lattice-matched quantum-confined layers with tensile-strained layers to obtain both TE and TM optical signals. All the active layers are based on a single (pure) quantum-confined structure, typically like quantum wells. Such active structures have a distinct limitation in the depolarization bandwidth because it is determined by the intrinsic property of a quantum-confined structure. This restricts depolarization applications, as broadband depolarization is more desirable for more polarization-insensitive optical applications. Although different band-gaps of materials can be applied in the active structure to broaden the depolarization bandwidth,[26,28] it is actually difficult to obtain a uniform and very wide gain spectrum in both TE and TM modes because it is difficult to finely control the multiple quantum-confined layer growths with different parameters and the numbers of quantum-confined layers that can be used in a single chip are also limited.

Recently, hetero-dimension-hybrid quantum structures were proposed to improve depolarization-relevant effects. Among them, the quantum well–dot-coupled structure is a typical example, with which depolarization can be achieved over a wider spectral range.[29] This offers a new route to realize broadband depolarization. Unfortunately, the poor energy storage capacity and irregularity of the dots restrict this kind of hybrid quantum structure as a promising candidate in realizing broadband depolarization.[30,31]

In view of the above considerations, we are proposing a novel depolarization solution and the corresponding quantum structure to realize ultra-broadband depolarization for strained light-emitting diodes. It is based on a kind of quantum well–wire-hybrid nanostructure recently proposed by our group,[32,33] where the quantum wires are formed directly on the well in a self-assembling way. This hybrid quantum-confined structure has displayed some special advantages over traditional quantum wells or dots. However, as it is a new material structure, many of its physical properties and relevant mechanisms that may be different from those of traditional quantum structures are still unknown and have not been widely investigated so far. Previous research on this hybrid quantum-confined nanostructure focused mainly on its gain-broadening (super-gain) property due to the joint role of well and wires,[32] as well as the improvement in the high-temperature performance of the device due to the reduction in non-radiative recombination under the action of quantum wires.[33] Recently, a distinguished depolarization property due to wire-to-well strain modulation in this well–wire-hybrid nanostructure was observed in our experiments for the first time. This depolarization effect is associated with an interesting quantum well–wire interaction mechanism, which is different from traditional ones and has not been reported in any previous literature. This mechanism introduces a certain tensile strain to the compressive-strain-dominant InGaAs well via the well–wire interface and leads to hybrid-strain status in the structure. It therefore changes the HH and LH energy-band distributions in the material structure and relative emission intensities between TE and TM modes. Therefore, this brings about a new possibility of realizing independent bipolarization for polarization-insensitive light-emitting diodes. Moreover, the aliasing effect of the directly-coupled well and wires also makes it possible to increase the depolarization bandwidth. Finally, we propose a quantum well–wire-hybrid nanostructure instead of well–dot-hybrid ones here, because quantum wires can have better energy storage capacity and regularity than dots. The relevant analysis and discussion are given in the following sections.

# Material structure and characterization

## Material structure and fabrication

The material structure used here is similar to that described in references 32 or 33. It consists of a typical InGaAs/GaAs/GaAsP material system, as illustrated in Fig. 1(a). The active structure contains a 10 nm-thick InGaAs quantum well and a layer of 2 nm-high (statistical average) InGaAs quantum wires that are formed on the well surface in a self-assembling way. Thus, the well and wires constitute a directly-coupled hybrid quantum structure. This is achieved by utilizing the orientation-dependent on-GaAs multi-atomic step effect in the material growth.[32–34] A high In-content of 0.17 is applied for the InGaAs active structure (including the well and wires), ensuring that the strain-driven In-segregation effect would occur and promoting In-atom migration under the In-segregation effect during the material growth.[35,36] Owing to the In-segregation effect, the In-contents in both well and wires would vary continuously along the growth direction, resulting in the band-gap of the active structure changing accordingly. This effect also makes it possible to form higher In-content in the directly-coupled wires than in the well.[37] This means that the lattice constant of the quantum wires would be larger than that of the well at the well–wire interface,[38] and thus tensile stress would be introduced to the well. These are the foundations for realizing ultra-broadband depolarization. Beyond the active structure (well and wires) are the 2 nm-thick GaAs strain-buffer-layers and 8 nm-thick $GaAs_{0.92}P_{0.08}$ barriers. The InGaAs/GaAs/GaAsP kernel is covered by 2 μm-thick AlGaAs waveguide layers.

The whole epitaxial structure is grown on the GaAs (001) substrate at slight misorientation under 100 mbar at the V/III ratio of 50 via metal–organic chemical vapor deposition (MOCVD, aix200/4) using trimethylgallium (TMGa), trimethyl-indium (TMIn), trimethylaluminium (TMAl), arsine ($AsH_3$), and high-purity hydrogen ($H_2$) carrier gas. The deposition process is at a rate of 1 μm h$^{-1}$, a high temperature of 650 °C, and a total flow rate of 13 slm. The high temperature in the
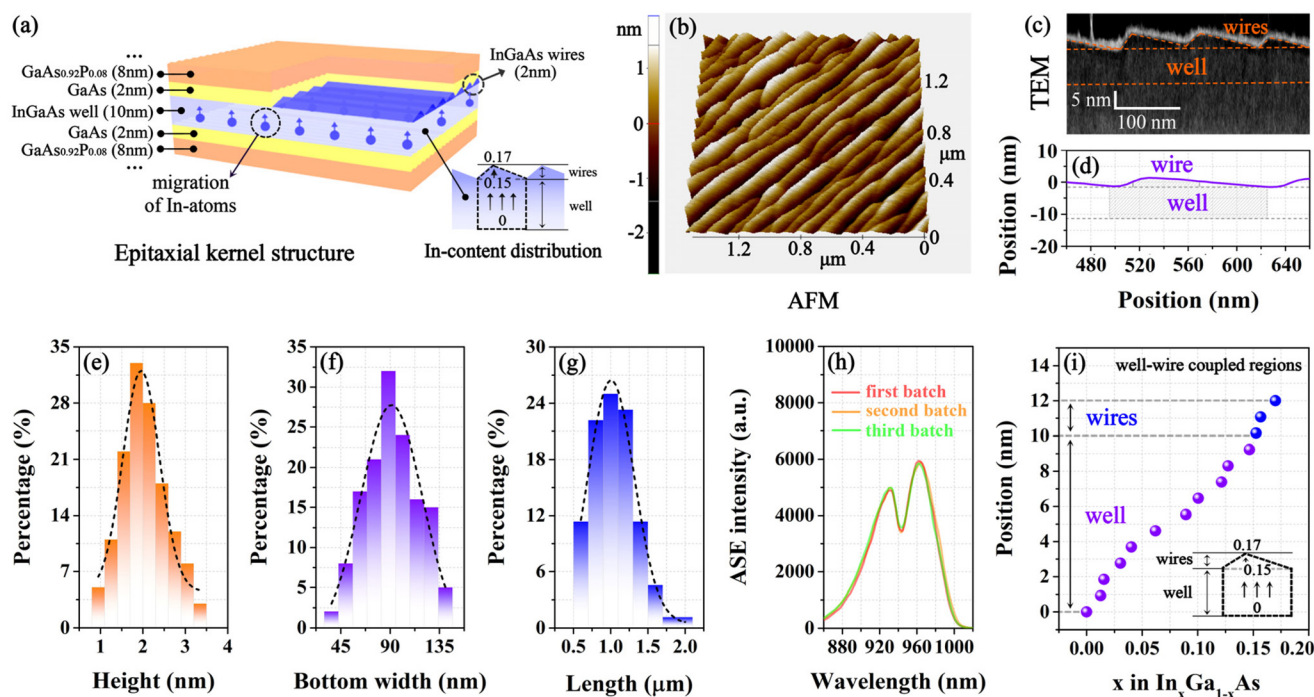
**Fig. 1** (a) Schematic illustration of the directly-coupled well–wire-hybrid nanostructure. (b) 3D-view of the on-well quantum wires from the AFM measurement. (c) The side-view of the well–wire-hybrid structure from the TEM measurement. (d) The cross-section of wires from AFM line scanning. Statistical distributions of (e) height (orange pillars), (f) bottom width (purple pillars), and (g) length (blue pillars) of the wires in Gaussian fitting (dashed lines) by measuring 140 wires at random. (h) The unpolarized ASE spectra of three different batches of samples fabricated under the same growth conditions and measured in the same pump environment. (i) The change in In-content at different positions of the active material and the distribution of In-content in the directly-coupled well–wire regions based on the XPS measurement.

material growth can also increase the migration length of the In atoms.

**Structural characterization**

The quantum wires formed on the well in the quantum well–wire-hybrid nanostructure were characterized through a special sample with an exposed InGaAs upper surface, which was fabricated under the same growth conditions by terminating its epitaxial growth process just after obtaining the complete InGaAs layer. The wires were morphologically observed and measured with an atomic force microscope (AFM, XE100), as displayed in Fig. 1(b). The cross-sectional measurement of the well–wire structure with a cross-sectional transmission electron microscope (X-TEM, JEM-2100F) shows that the cross-section of wires presents a triangle-like distribution with a very small base-angle and a large top-angle, as displayed in Fig. 1(c), in which the well and wires are highlighted with orange dashed lines and a white contour line along the wires is formed from focused-ion-beam (FIB) treatment of the sample cross-section. Below the white contour line are the wire and well layers. The cross-sectional feature of the wires was also confirmed by scanning the AFM image along the direction perpendicular to the wires in Fig. 1(b). The result is shown in Fig. 1(d). It indicates that the effective area of the quantum wires does not fully cover the well surface; that is, the wires

can be considered to present a distribution in a fixed space. Therefore, the overall nanostructure can be composed of two parts. One involves the directly-coupled well and wire regions. The other one involves the pure-well regions without the wires. Owing to the absence of the wire-to-well quantum modulation role in the pure-well regions, the directly-coupled well–wire-hybrid regions will play a key role in depolarization and bandwidth broadening. The pure-well regions are equivalent to a reference well.

Statistical analysis of the wires shows that the wire height is between 1 nm and 3 nm, the bottom width of the wires is between 50 nm and 140 nm, and the wire length varies between 0.5 μm and 2 μm based on a random selection of 140 wires from the AFM measurement results. The results fit the Gaussian distributions centred at 2.0 nm, 90 nm, and 1.0 μm, respectively, as displayed in Fig. 1(e)–(g). Although the self-assembled quantum wires formed on the well are not very regular in size or distribution, the macroscopic repeatability and stability of the whole structure performance are indubitable. We measured the amplified spontaneous emission (ASE) spectra of three different batches of samples fabricated under the same growth conditions for this purpose. In addition, the ASE spectra can also reflect the polarization variation of a quantum-confined structure from peak intensities and wavelengths. The measurement result is shown in Fig. 1(h).

Obviously, the three measured ASE spectra show very good consistency. Therefore, the slight non-uniformity of the wires does not affect the polarization performance of the well–wire hybrid nanostructure. In addition, owing to the anisotropic properties of quantum wires, the ASE intensity is related to the wire direction for an edge-emitting device. It can reach a maximum along the direction parallel to the wires.[39,40] Therefore, all the ASE measurements in our experiment take the direction parallel to the wires to obtain the maximum ASE intensities. The In-content (the $x$-value in $In_xGa_{1-x}As$) of the whole hybrid quantum structure varies monotonically from 0 to 0.15 in the well and from 0.15 to 0.17 in the wires along the material growth direction, according to the measurement results of X-ray photoelectron spectroscopy (XPS, PHI Quantera II) of the sample, as shown in Fig. 1(i). This fits well with the result from the strain-driven In-segregation effect. All the above structural characterization data are consistent with our previous research results.[32,33]

## Depolarization results and discussion

### Depolarization of spontaneous emission

The experimental setup for the ASE measurement is illustrated in Fig. 2. The sample is processed in an edge-emitting configuration. In order to collect polarized light signals, a linear polarizer P and two lenses $L_1$ and $L_2$ are used. The TE-polarized light signal is measured by setting the polarizer in the in-plane (horizontal) direction, whereas the TM-polarized light signal is collected in the vertical (material growth) direction. The optical signals are detected using a spectrometer (HR4000CG-UV-NIR) coupled with a fiber. A beam from an 808 nm pulsed-laser (LWIRL808-40W-F) with a pulse width of 20 ms and frequency of 1 Hz is used to optically pump the sample from the top in the experiment.

Firstly, the unpolarized ASE spectrum is measured under an injection power of 197 mW at 298 K to look at the general emission of the hybrid quantum structure, as shown in Fig. 3(a). We find that the measured ASE spectrum can be fitted well with the bi-Gaussian function with peaks at 932 nm (peak A) and 967 nm (peak B). Owing to the one-dimensional quantum wires combining directly with the well in the directly-coupled well–wire regions, the band-gap is increased in this part compared with the pure-well part of the

nanostructure.[32,41] Thus, peak A in the ASE spectrum in Fig. 3(a) comes from the directly-coupled well–wire region emission, while peak B is generated by the pure-well regions of the whole nanostructure.

In general, the light-emitting intensity from an active region is proportional to the active region area. Thus, we can approximately determine the spatial proportion of parallel pure-well regions and well–wire-hybrid regions by measuring ASE spectra of the two types of region and comparing the integrated peak intensities of two ASE spectra. As a result, the ASE peak intensities as functions of the injection power for the pure-well regions and the well-wire-hybrid regions are measured and given in Fig. 3(b). It is shown from Fig. 3(b) that the proportion (black curve) of ASE peak intensities from the pure-well and well–wire-hybrid region emissions is about 2.0, even if the injection power is changed. Therefore, we can conclude that the spatial proportion of the pure-well and well–wire-hybrid regions is approximately 2 : 1.

The polarization transition between TM and TE modes in the ASE spectrum is recorded in Fig. 3(c), which is obtained by rotating the polarizer under a fixed injection power of 165 mW at 298 K. We define TM polarization as corresponding to 0° (or 180°) of the polarizer angle, *i.e.* the vertical direction of the magnetic-field vector, and TE polarization as corresponding to 90° of the polarizer angle, *i.e.* the vertical direction of the electric-field vector. So bi-Gaussian fitting curves of the TE and TM ASE spectra from the directly-coupled well–wire-hybrid part and the pure-well part of the whole nanostructure are obtained, which are shown in Fig. 3(d) and (e). This result shows that the comparable TE and TM emission intensities occur from the well–wire-hybrid part, but the TE emission is in absolute dominance from the pure-well part.

To further study different polarization characteristics of the TE and TM emissions from the well–wire-hybrid part and the pure-well part in the whole nanostructure, the peak wavelengths of the spectra as the function of the polarizer angle are analyzed by rotating the polarizer and recording the ASE spectra. The results are obtained in Fig. 3(f) and (g). In addition, the integrated-peak-intensities of ASE spectra as the functions of the polarizer angle were also measured and are displayed in Fig. 3(h) and (i). The results show that the variations in peak wavelengths and integrated-peak-intensities in
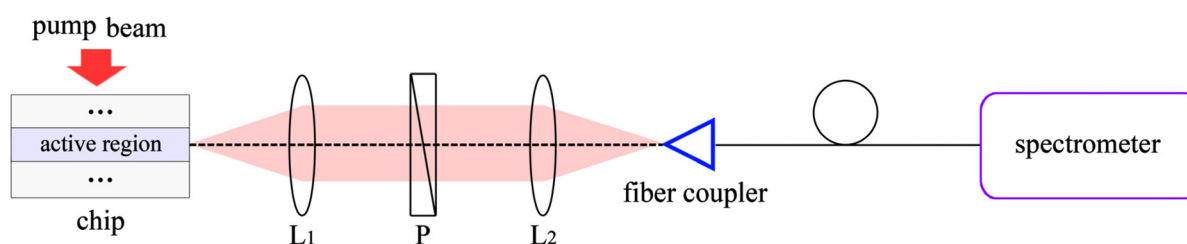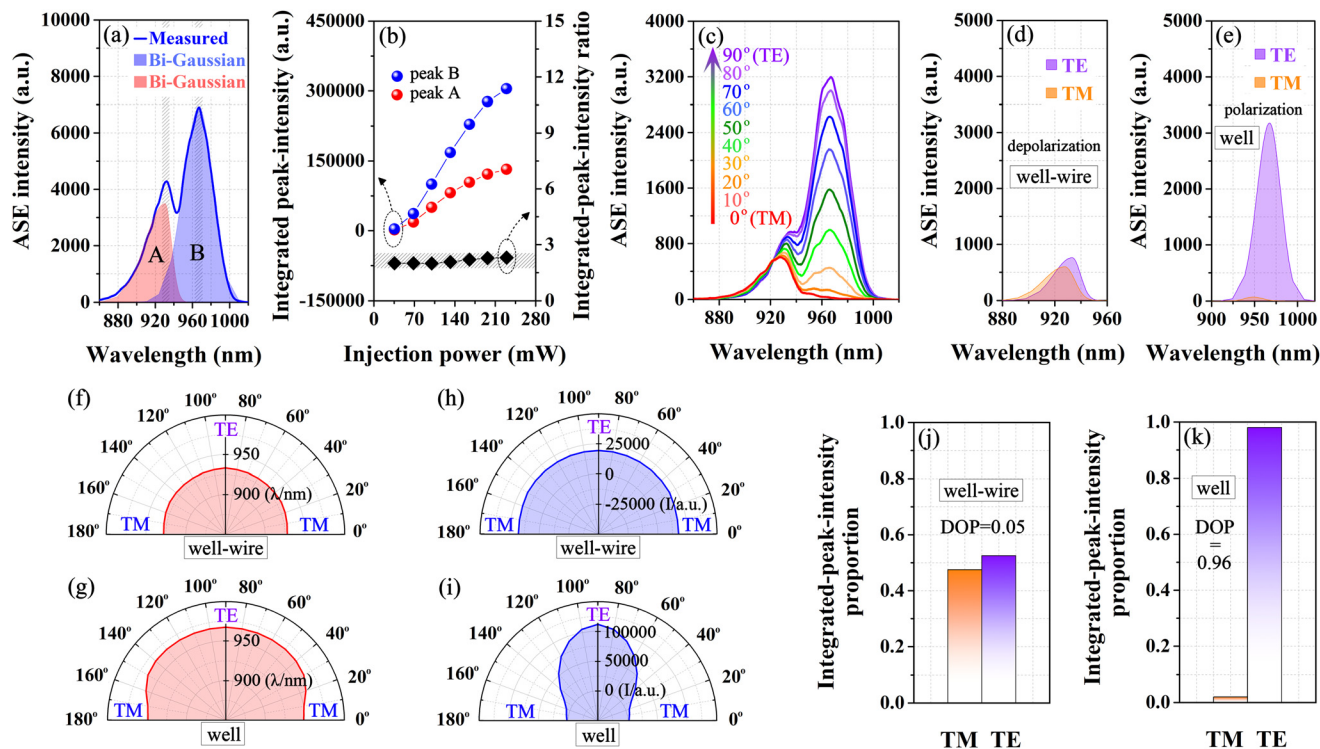


**Fig. 2** Experimental setup for polarized-ASE measurement of an edge-emitting sample.

**Fig. 3** (a) ASE polarization analysis with the experimental data and the bi-Gaussian fittings. (b) The integrated ASE peak-intensities of peak B (blue curve) and peak A (red curve) *versus* injection power, and their ratio peak B/peak A (black curve). (c) The changes in ASE-peak positions and intensities with varying polarization from TM to TE modes under an injection power of 165 mW and a temperature of 298 K. (d) and (e) Bi-Gaussian fitting of ASE spectra at different polarization modes. (f) and (g) Peak wavelength variations of ASE spectra as a function of polarizer angle in polar coordinates. (h) and (i) The integrated peak-intensity variations as a function of polarizer angle in polar coordinates. (j) and (k) The integrated peak-intensity proportions of TM and TE polarizations, where (d), (f), (h) and (j) are the results from the well−wire regions and (e), (g), (i) and (k) are the results from the pure-well regions.

polarization are tiny for the emission from the well–wire-hybrid part and huge for the emission from the pure-well part. Thus, it can be inferred that the emission signals from the directly-coupled well–wire-hybrid part of the nanostructure are polarization insensitive. These results can also be illustrated by the degree of polarization (DOP), defined as[42–44]

$$DOP = \frac{I_{TE} - I_{TM}}{I_{TE} + I_{TM}} \qquad (1)$$

where $I_{TE}$ and $I_{TM}$ represent the integrated intensities of the ASE peaks in TE and TM modes, respectively. With the data in Fig. 3(h) and (i), the DOP values are 0.05 and 0.96 for the emissions from the well–wire-hybrid part and the pure-well part, respectively, under an injection power of 165 mW and a fixed temperature of 298 K. As shown in Fig. 3(j), the very close TE and TM emission intensity proportions indicate that significant depolarization takes place in the well–wire-hybrid part due to wire-to-well modulation in the nanostructure. In contrast, the TE emission intensity is far larger than the TM emission intensity, as the integrated TM peak-intensity holds only 2% of the peak-intensity for pure-well emission, as displayed in Fig. 3(k). The depolarization efficiency ($\eta_1$) in the directly-coupled well–wire-hybrid part rises by 95%, compared with the

pure-well emission without the wire-to-well modulation, which is obtained from the following formula:

$$\eta_1 = \left| \frac{DOP_{well-wire} - DOP_{well}}{DOP_{well}} \right|. \qquad (2)$$

When the injection power is increased, the integrated TE and TM peak-intensities from the well–wire-hybrid part emissions rise and gradually saturate, as shown in Fig. 4(a). It can be seen that the TE and TM peak-intensities remain nearly the same the whole time, *i.e.* the very low DOP value throughout this process. This also indicates the high stability of depolarization at different injection levels for the quantum well–wire-hybrid system.

Furthermore, we also studied the temperature-dependent depolarization behavior of the well–wire-hybrid part of the nanostructure using the polarized ASE bi-Gaussian fitting spectra in Fig. 4(b) under a fixed injection power of 165 mW. It can obviously be seen from Fig. 4(b) that the TM-polarized emission decays more slowly with temperature than the TE-emission for the well–wire-hybrid part. As the temperature rises from 290 K to 320 K, the TE-peak goes down quickly and tends towards the TM-peak value, *i.e.* the DOP is reduced, as
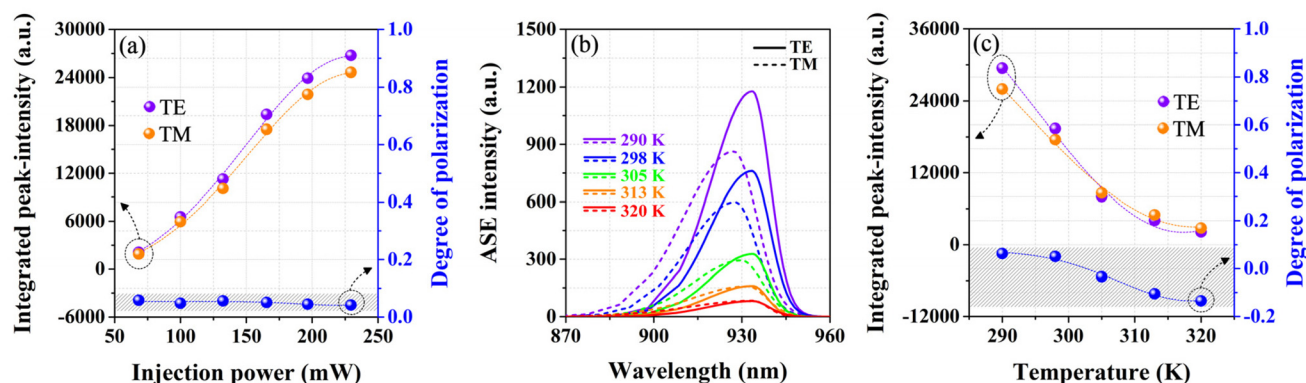
**Fig. 4** (a) TE and TM peak-intensities of peak A in Fig. 3(a) and the corresponding DOP as a function of injection power. (b) Bi-Gaussian fitting of the polarized ASE spectra for the well–wire-hybrid regions with various temperatures of 290–320 K at an injection power of 165 mW. (c) TE and TM peak-intensities of peak A and the corresponding DOP as a function of temperature.

illustrated in Fig. 4(c). This result indicates that the depolarization effect will be further improved, as the device temperature is increased. When the temperature is ~305 K, the DOP reaches a minimum, *i.e.* the best depolarization is obtained. With a further increase in temperature, the TE emission will become weaker than the TM emission and DOP shows a negative value. The temperature-dependent variation in DOP may be because TM polarization is more sensitive to inhomogeneous thermal strain induced effect for such a well–wire hybrid quantum structure.[44]

### Depolarizing and broadening of optical gain

Gain depolarization plays a key role in polarization-insensitive optical amplification. With the ASE spectra measured at two ends of an edge-emitting sample and the following equation,[45] the polarized modal gains of the quantum well–wire-hybrid structure can be obtained. The gain measurement principle is briefly illustrated in Fig. 5(a).[32]

$$G = \frac{1}{L} \ln \frac{(1 - R_2) \times I_{ASE1} - I_{ASE2}}{R_2 \times I_{ASE2}} \quad (3)$$

where $L = 1.5$ mm is the single-pass distance of light propagating through the sample. $R_1$ and $R_2$ denote the reflectivity of the two end-surfaces of the sample, where the $R_1$-end is coated with reflectivity of $R_1 \approx 0$ and the $R_2$-facet is uncoated. Thus, the reflectivity of the $R_2$-facet is determined by the material indices, which is $R_2 \approx 30\%$ for the InGaAs material. $I_{ASE2}$ denotes the ASE intensity detected at the $R_2$-end of the experimental sample, which is associated with the reflectivity ($R_2$). $I_{ASE1}$ denotes the ASE intensity detected at the $R_1$-end, which is the intensity superposition of the single-pass light through the $R_1$-end and the round-trip light reflected by the $R_2$-facet end. The gain measurement result is shown in Fig. 5(b).

In Fig. 5(b), the TE (purple dotted line) and TM (orange dotted line) modal gains present not only similar distributions, but also greatly-broadened gain bandwidth under an injection power of 165 mW at 298 K. The full width at half-maximum (FWHM) reaches 73 nm (from 877 nm to 950 nm). In general, the gain bandwidth (FWHM) of a single InGaAs quantum well is 30 nm.[46] Due to the increase in quantum confinement, the energy-level spacings in the quantum wires are larger than that in a well for the same material composition.[41] The unified conduction and valence bands with larger energy-level spacings than those in a pure well and smaller than those in the wires would be formed in the quantum structure, where the well and wires combine together in a directly-coupled way.
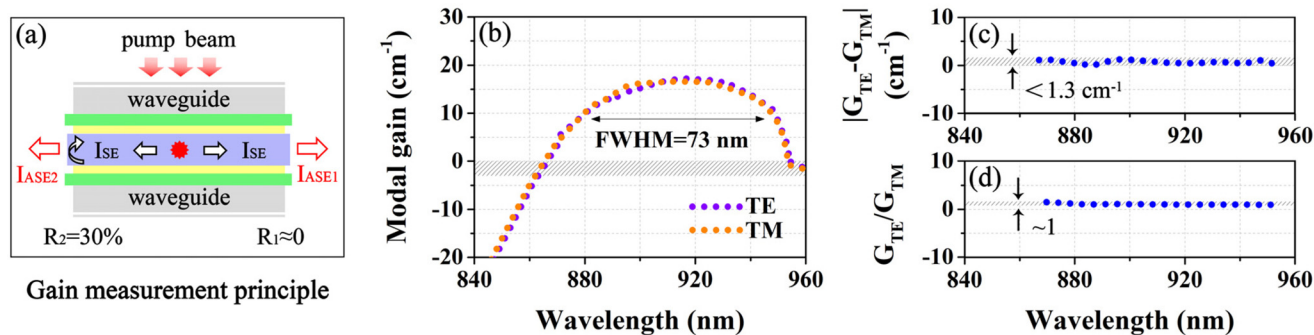


**Fig. 5** (a) A diagram of the gain measurement principle with an optically-pumped edge-emitting sample. (b) TE (purple dotted line) and TM (orange dotted line) modal gains of the well–wire-hybrid regions. (c) Gain difference between TE and TM polarizations. (d) The ratio of TE and TM gains.

Since this aliasing effect between directly-coupled quantum wires and well changes the energy-level distribution of the whole nanostructure, the density-of-states will also be changed. Thus, carrier recombination will be generated over a wider energy-band range, so that the gain bandwidth is broadened. In addition, the slight size fluctuations and special shape (triangle-like cross-section) of the quantum wires may also play a role in broadening and homogenizing the gain distribution. Furthermore, the difference in TE and TM gains is $|G_{TE} - G_{TM}| < 1.3$ cm$^{-1}$, as shown in Fig. 5(c). Therefore, the ratio of TE and TM gains is $G_{TE}/G_{TM} \approx 1$ over a broad wavelength range of 80 nm (from 870 nm to 950 nm), as illustrated in Fig. 5(d). This result shows that the TM gain amazingly reaches the TE gain level in an InGaAs compressive-strained quantum structure. This means that the independent and comparable bipolarization of optical amplification may be realized. These results indicate that excellent depolarization would occur over a very broad spectral range with a quantum well–wire-hybrid nanostructure due to quantum wire-to-well modulation and their aliasing effect.

### Depolarization mechanism of quantum wire-to-well modulation

The depolarization mechanism in the quantum well–wire-hybrid nanostructure is associated with the introduction of tensile strain within the well under wire modulation. In a typical GaAs/InGaAs/GaAs material system, owing to lattice mismatch between InGaAs and GaAs layers, the larger InGaAs lattice is biaxially compressed (perpendicular to the growth direction) to match the GaAs one and vertically stretched (along the growth direction). Thus, the HH band is higher than the LH band and carrier recombination mainly takes place between the conduction band and the HH band in the InGaAs layer, resulting in stronger TE-polarized emission than TM emission.

However, the incorporation of wires into the well in a direct-coupling pattern leads to a change in strain nature and status for the well. Since the In-content in the wires is higher than that in the well from the In-segregation effect in the process of material growth,[37] the lattice constant of the wires will be larger than that of the well.[38] This leads to tensile-stress being generated in the compressive-strained well layer beneath the wire/well interface, as illustrated in Fig. 6(a). Therefore, it partially counterbalances the compressive-strain in the well. In the energy-band structure of the system, the tensile-strain will raise the LH band, so that the energy difference between the HH and LH bands will be reduced. This is a peculiar status in a strained structure, *i.e.* there exist both compressive and tensile strains, whose joint roles make up a special energy-band distribution with closer LH and HH bands in the whole nanostructure.

In order to understand the quantum wire-to-well modulation effect in the InGaAs hybrid quantum regions, the well–wire-constructed hybrid-energy-band structure is drawn in Fig. 6(b). In contrast, Fig. 6(c) shows the energy-band structure of the InGaAs pure well with the same In-content variation. The step barriers in the energy-band structure are formed due to the GaAs strain-buffer-layers and the GaAs$_{0.92}$P$_{0.08}$ barrier-layers. Since the band-gap is changed continuously for both well and wires from the In-segregation effect, their band-edges are inclined, as shown in Fig. 6(b) and (c). The slight tilt of the right-hand barrier in the energy-band structure is because of a few In atoms penetrating into the adjacent GaAs strain-buffer layer under the In-segregation effect.

In general, the first conduction band ($C_1$) in quantum wires is higher than that in a well for the same material composition.[41] However, a unified $C_1$-band would be formed in the quantum structure where the well and wires combine together in a directly-coupled way. This means that the $C_1$-band in the well rises and the $C_1$-band in the wires drops to reach a balance, as displayed in Fig. 6(b).

Similarly, the unified first heavy-hole (HH$_1$) and first light-hole (LH$_1$) bands are also formed in the quantum well–wire-hybrid structure. Therefore, it makes the carriers redistribute in the conduction band and the valence band. Since tensile-strain is introduced to the compressive-strained well under the
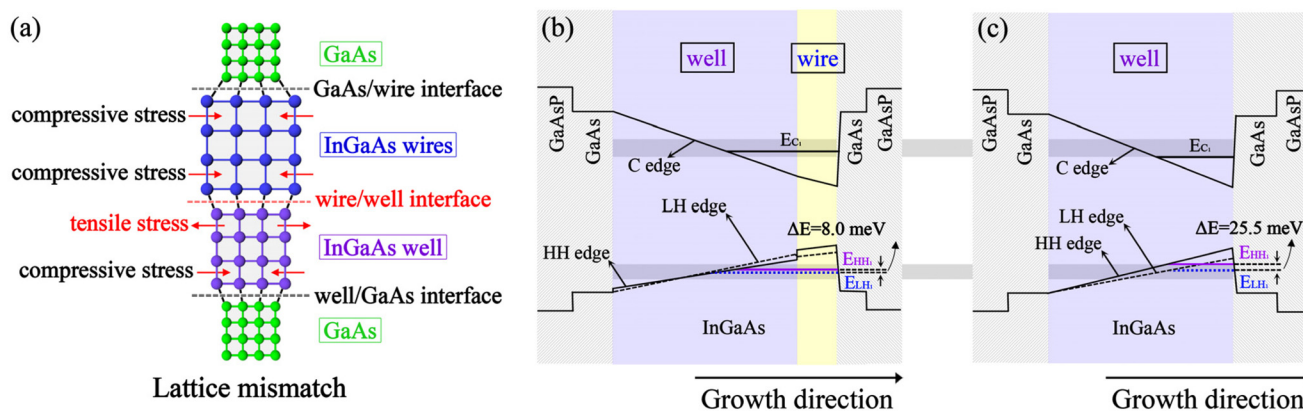


**Fig. 6** (a) A diagram of lattice mismatch of the directly-coupled well–wire-hybrid structure. (b) and (c) Energy-band structures of the well–wire-hybrid regions and the pure-well regions in the whole nanostructure, respectively.

action of the wires, the degeneracy of the $HH_1$ and $LH_1$ bands is enhanced, *i.e.* the $HH_1$ band shifts downwards and the $LH_1$ band moves upwards compared to the pure compressive-strained well. In addition, unlike the pure well, the HH and LH band edges have different potential gradients due to the built-in strain variation through the well in the directly-coupled well–wire structure, as shown in Fig. 6(b). Therefore, the quantum well–wire-hybrid structure can produce comparable TE and TM gains and emissions, which correspond to the carrier recombination between $C_1$ and $HH_1$ bands and the carrier recombination between $C_1$ and $LH_1$ bands, respectively. With the experimental data of ASE peak wavelengths at different polarization modes in Fig. 3(f) and (g), the energy differences between the $HH_1$ band and the $LH_1$ band can be calculated, which are obtained to be $\Delta E = 25.5$ meV for the pure-well regions and $\Delta E = 8.0$ meV for the well–wire-hybrid regions. The corresponding wavelength difference of TE- and TM-polarized ASE peaks is 18.9 nm from the pure-well region emission. However, the wavelength difference of TE- and TM-polarized ASE peaks is only 5.6 nm from the well–wire-hybrid region emission. The latter is much less than the former. The degeneracy of $HH_1$ and $LH_1$ bands is increased by $\eta_2 = 69\%$, compared with the $HH_1$ and $LH_1$ bands in the pure well. Therefore, it confirms the above analysis. The calculation is done with the following equation.

$$\eta_2 = \left| \frac{(\Delta E_{\text{well-wire}} - \Delta E_{\text{well}})}{\Delta E_{\text{well}}} \right| \tag{4}$$

Under the role of the directly-coupled well and wires, an InGaAs hybrid quantum system with ultra-broadband and independent-polarization properties is constructed, providing a flexible ultra-broadband depolarization approach for polarization-insensitive light-emitting diode applications.

## Conclusions

In summary, we describe a new discovery of an ultra-broadband depolarization mechanism that exists in the newly-proposed quantum wire–well-hybrid nanostructure and the corresponding realization approach of ultra-broadband depolarization for polarization-insensitive light-emitting diode applications. The mechanism is associated with the directly-coupled quantum well and wire interaction and their aliasing effect in the wire–well-hybrid quantum system. By utilizing the In-segregation and the growth-orientation-dependent multi-atomic step effects, the on-well wires hold higher In-content than the well, so that a larger lattice constant is formed in the wires than in the well. Therefore, the tensile-strain is incorporated into the compressive-strain well *via* the well–wire interface under the action of the wires. This leads to the degeneracy of the $HH_1$ and $LH_1$ bands in the well. Thus, energy-band depolarization is formed. Meanwhile, energy-band redistribution due to the aliasing effect of the directly-coupled well and wires greatly broadens the depolarization bandwidth in a single chip. The results indicate that hetero-dimension-hybrid

nanostructures will be a new way to realize ultra-broadband and polarization-insensitive light-emitting diode applications.

## Author contributions

Yuhong Wang: Investigation, data curation, formal analysis, writing – original draft. Hanxu Tai: Investigation, formal analysis, validation. Ruonan Duan: Investigation, formal analysis. Ming Zheng: Investigation, writing – review & editing. Yue Shi: Investigation, data curation. Jianwei Zhang: Validation, writing – review & editing. Xing Zhang: Formal analysis, writing – review & editing. Yongqiang Ning: Investigation, writing – review & editing. Jian Wu: Conceptualization, funding acquisition, writing – review & editing.

## Conflicts of interest

There are no conflicts to declare.

## Acknowledgements

## References

1 N. Mendelson, M. Doherty, M. Toth, I. Aharonovich and T. T. Tran, *Adv. Mater.*, 2020, **32**, 1908316.

2 T. Liu, H. Li, X. H. Liu, Y. Wang, Y. N. Guo, S. F. Wang, G. S. Fu, Y. I. Mazur, M. E. Ware, G. J. Salamo and B. L. Liang, *Appl. Surf. Sci.*, 2023, **636**, 157876.

3 G. O. Eren, S. Sadeghi, H. B. Jalali, M. Ritter, M. Han, I. Baylam, R. Melikov, A. Onal, F. Oz, M. Sahin, C. W. Ow-Yang, A. Sennaroglu, R. T. Lechner and S. Nizamoglu, *ACS Appl. Mater. Interfaces*, 2021, **13**, 32022–32030.

4 H. B. Shen, W. R. Cao, N. T. Shewmon, C. C. Yang, L. S. Li and J. G. Xue, *Nano Lett.*, 2015, **15**, 1211–1216.

5 B. K. SaifAddin, A. S. Almogbel, C. J. Zollner, F. Wu, B. Bonef, M. Iza, S. Nakamura, S. P. DenBaars and J. S. Speck, *ACS Photonics*, 2020, **7**, 554–561.

6 H. D. Sun, M. K. Shakfa, M. M. Muhammed, B. Janjua, K. H. Li, R. H. Lin, T. K. Ng, I. S. Roqan, B. S. Ooi and X. H. Li, *ACS Photonics*, 2018, **5**, 964–970.

7 Y. H. Won, O. Cho, T. Kim, D. Y. Chung, T. Kim, H. Chung, H. Jang, J. Lee, D. Kim and E. Jang, *Nature*, 2019, **575**, 634–638.

8 E. M. Pavelescu, T. Jouhti, C. S. Peng, W. Li, J. Konttinen, M. Dumitrescu, P. Laukkanen and M. Pessa, *J. Cryst. Growth*, 2002, **241**, 31–38.

9 J. Zhang, Y. Xu, Y. Jiang, L. Bai, H. Chen, J. Li, L. Wang, W. Wu and G. Song, *Nanoscale*, 2018, **10**, 12657–12664.

10 Y. H. Zhu, H. Y. Yu and W. J. Fan, *Appl. Phys. Lett.*, 2011, **98**, 121112.

11 P. Koonath, S. Kim, W. Cho and A. Gopinath, *IEEE J. Quantum Electron.*, 2002, **38**, 1282–1290.

12 N. Yasuoka, H. Ebe, K. Kawaguchi, M. Ekawa, S. Sekiguchi, K. Morito, O. Wada, M. Sugawara and Y. Arakawa, *J. Lightwave Technol.*, 2012, **30**, 68–75.

13 H. Ma, S. Chen, X. Yi, G. Zhu and J. Jin, *Opt. Quantum Electron.*, 2004, **36**, 551–558.

14 C. Guo, C. Sun, Z. Hao and Y. Luo, *Jpn. J. Appl. Phys.*, 2000, **39**, 6166–6169.

15 D. Ahn and T. K. Yoo, *Appl. Phys. Lett.*, 1992, **60**, 548–550.

16 L. R. Huang, Ph.D. Thesis, Huazhong University of Science & Technology, Wuhan, P. R. China, 2005.

17 K. Magari, M. Okamoto, Y. Suzuki, K. Sato, Y. Noguchi and O. Mikami, *IEEE J. Quantum Electron.*, 1994, **30**, 695–702.

18 S. J. Liu, Y. Zhou, S. Zhou, C. P. Mo, H. Zhao, S. H. Ding, K. Tian and Z. R. Tang, *J. Mater. Sci.: Mater. Electron.*, 2018, **29**, 10102–10108.

19 Y. Cho and W. Y. Choi, Proc. of SPIE 3944, 2000, 181–189.

20 M. S. Wartak and P. Weetman, *IEEE Photonics Technol. Lett.*, 2004, **16**, 996–998.

21 J. Yin, G. Du, S. Liu, Z. Liu, X. Wang, Z. Li, Z. Yin and S. Yang, *Opt. Laser Technol.*, 2002, **34**, 595–597.

22 A. Mathur and P. Daniel Dapkus, *Appl. Phys. Lett.*, 1992, **61**, 2845.

23 L. F. Tiemeijer, P. J. A. Thijs, T. van Dongen, R. W. M. Slootweg, J. M. M. van der Heijden, J. J. M. Binsma and M. P. C. M. Krijna, *Appl. Phys. Lett.*, 1993, **62**, 826.

24 S. J. Bae, S. H. Park and Y. T. Lee, *Opt. Quantum Electron.*, 2003, **35**, 967–977.

25 T. Kita, O. Wada, H. Ebe, Y. Nakata and M. Sugawara, *Jpn. J. Appl. Phys.*, 2002, **41**, L1143–L1145.

26 K. Kawaguchi, M. Ekawa, N. Yasuoka, T. Akiyama, H. Ebe, M. Sugawara and Y. Arakawa, *Phys. Status Solidi C*, 2006, **3**, 3646–3651.

27 K. Kawaguchi, N. Yasuoka, M. Ekawa, H. Ebe, T. Akiyama, M. Sugawara and Y. Arakawa, *Jpn. J. Appl. Phys.*, 2006, **45**, L1244–L1246.

28 J. Nkanta, R. Maldonado-Basilio, S. Abdul-Majid, J. Zhang and T. Hall, *Proc. SPIE*, 2014, **9007**, 900708.

29 L. R. Huang, Y. Yu, P. Tian and D. X. Huang, *Semicond. Sci. Technol.*, 2009, **24**, 015009.

30 P. B. Joyce, T. J. Krzyzewski, G. R. Bell and T. S. Jones, *Phys. Rev. B: Condens. Matter Mater. Phys.*, 2000, **62**, 10891–10895.

31 S. K. Jana, P. Mukhopadhyay, S. Kabi, N. N. Halder, A. Bag, S. Ghosh and D. Biswas, *IEEE Trans. Nanotechnol.*, 2014, **13**, 917–925.

32 Y. H. Wang, H. X. Tai, R. N. Duan, M. Zheng, W. Lu, Y. Shi, J. W. Zhang, X. Zhang, Y. Q. Ning and J. Wu, *Nanophotonics*, 2023, **12**, 1763–1776.

33 H. X. Tai, Y. H. Wang, R. N. Duan, M. Zheng, W. Lu, Y. Shi, J. W. Zhang, X. Zhang, Y. Q. Ning and J. Wu, *J. Phys. D: Appl. Phys.*, 2023, **56**, 23LT01.

34 S. Lee, M. Akabori, T. Shirahata, K. Takada, J. Motohisa and T. Fukui, *J. Cryst. Growth*, 2001, **231**, 75–81.

35 A. S. Sozykin, S. S. Strelchenko, E. V. Prokolkin and M. A. Ladugin, *J. Cryst. Growth*, 2013, **363**, 253–257.

36 H. Yu, C. Roberts and R. Murray, *Appl. Phys. Lett.*, 1995, **66**, 2253–2255.

37 S. Martini, A. A. Quivy, M. J. da Silva, T. E. Lamas, E. C. F. da Silva and J. R. Leite, *J. Appl. Phys.*, 2003, **94**, 7050–7052.

38 S. Kang and T. S. Jeong, *J. Korean Phys. Soc.*, 2020, **76**, 231–236.

39 T. T. Zou, B. Zhao, W. Xin, F. Y. Wang, H. B. Xie, Y. H. Li, Y. W. Shan, K. Li, Y. B. Sun and J. J. Yang, *Nano Res.*, 2022, **15**, 4490–4499.

40 S. Hara, J. Motohisa, T. Fukui and H. Hasegawa, *Jpn. J. Appl. Phys.*, 1995, **34**, 4401–4404.

41 M. Asada, Y. Miyamoto and Y. Suematsu, *IEEE J. Quantum Electron.*, 1986, **9**, 1915–1921.

42 M. Shan, Y. Zhang, T. B. Tran, J. Jiang, H. Long, Z. Zheng, A. Wang, W. Guo, J. Ye, C. Chen, J. Dai and X. Li, *ACS Photonics*, 2019, **6**, 2387–2391.

43 J. Liu, J. Wang, X. Sun, Q. Sun, M. Feng, R. Zhou, Y. Zhou, H. Gao, T. Liu, Z. Huang and H. Yang, *ACS Photonics*, 2019, **6**, 2104–2109.

44 P. Jayavel, T. Kita, O. Wada, H. Ebe, M. Sugawara, Y. Arakawa, Y. Nakata and T. Akiyama, *Jpn. J. Appl. Phys.*, 2005, **44**, 2528–2530.

45 M. L. Ma, J. Wu, Y. Q. Ning, F. Zhou, M. Yang, X. Zhang, J. Zhang and G. Y. Shang, *Opt. Express*, 2013, **21**, 10335–10341.

46 G. Tsvid, J. Kirch, L. J. Mawst, M. Kanskar, J. Cai, R. A. Arif, N. Tansu, P. M. Smowton and P. Blood, *IEEE J. Quantum Electron.*, 2008, **44**, 732–739.